Aalborg Universitet

AALBORG UNIVERSITY

Mixed alkaline earth effect in sodium aluminosilicate glasses

Kjeldsen, Jonas; Smedskjær, Morten Mattrup; Mauro, John C.; Youngman, Randall E.; Huang, Liping; Yue, Yuanzheng

Mixed alkaline earth effect in sodium aluminosilicate glasses

Jonas Kjeldsen [a], Morten M. Smedskjaer [a], John C. Mauro [b], Randall E. Youngman [b],
Liping Huang [c], Yuanzheng Yue [a],*

[a] Section of Chemistry, Aalborg University, DK-9000 Aalborg, Denmark
[b] Science and Technology Division, Corning Incorporated, Corning, NY 14831, USA
[c] Department of Mat. Sci. Eng., Rensselaer Polytechnic Institute, Troy, NY 12180, USA

ABSTRACT

While the mixed alkali effect has received significant attention in the glass literature, the mixed alkaline earth effect has not been thoroughly studied. Here, we investigate the latter effect by partial substitution of magnesium for calcium in sodium aluminosilicate glasses. We use Raman and NMR spectroscopies to obtain insights into the structural and topological features of these glasses, and hence into the mixed alkaline earth effect. We demonstrate that the mixed alkaline earth effect manifests itself as a maximum in the amount of bonded tetrahedral units and as a minimum in liquid fragility index, glass transition temperature, Vickers microhardness, and isokom temperatures (viz., the temperatures at $\eta = 10^{13.5}$ and $10^{12.2}$ Pa s). The observed minima in fragility, glass transition temperature, and isokom temperature are ascribed to bond weakening in the local structural environment around the network modifiers. We suggest that, since the elastic properties of the investigated system are compositionally independent, the minimum in Vickers microhardness is closely correlated to the minimum in isokom temperatures. Both of these properties are related to plastic flow and the translational motion of structural units, and hence both may be related to the same underlying topological constraints. This indicates that there might not be any significant difference in the onset of the rigid sub-T_g constraints for the investigated compositions.

© 2013 Elsevier B.V. All rights reserved.

1. Introduction

Most alkali-containing oxide glasses exhibit non-additive variations of certain properties when one alkali ion is substituted by another one. This phenomenon is known as the "mixed alkali effect" and is one of the most intriguing unsolved phenomena in glass science [1,2]. The mixed alkali effect especially manifests itself in non-additive discrepancies in transport properties, such as diffusion, conductivity, and viscosity. These properties are commonly referred to as dynamic properties, in contrast to static properties such as density, refractive index, and molar volume, all of which exhibit relatively small deviations from linearity [3,4].

The mixed alkali effect has been known for decades, yet over the past few years it is still drawing significant attention [1,5–10]. In contrast, the mixed alkaline earth effect has received relatively little attention. The mixed alkaline earth effect is phenomenologically analogous to the mixed alkali effect, i.e., it concerns substitution of one alkaline earth ion by another one. The influence of the mixed alkaline earth effect on glass properties is also analogous to that of the mixed alkali effect, i.e., deviations from linearity are observed for certain glass properties upon substitution of alkaline earth ions [4,11–14]. Since the mixed alkaline earth effect can affect the glass

properties in a non-predictive manner, it is important to study this effect from both scientific and technological points of views.

Although the structural and topological origins of the mixed alkali effect have been the subject of much experimental and modeling work, a thorough understanding of the effect is still lacking [9,15,16]. Despite making progress in interpreting the mixed alkali effect by establishing phenomenological and physical models such as the strong [17,18] and the weak [19–23] electrolyte models, the diffusion controlled relaxation model [24,25], and the jump diffusion model [26], the experimental findings can still not be completely explained by theory. Recently, the introduction of the dynamic structure model [27–30] has helped to establish a more coherent picture [9,10,31–33]. The dynamic structure model is based on an energy landscape approach, in which the unoccupied cationic sites initially are associated with a relatively high potential energy. As the previously unoccupied sites become occupied, the surrounding atoms in the glassy network are ordered. Consequently, different potential energies for these sites are created. When an ion leaves its site, the associated potential energy relaxes back to that of the unoccupied site. Thus, there exists a time window during which the occupation of this site by a similar ion is energetically favored. As the relaxation time and the potential energy associated with the ion site depend on the type of ion, each ion creates its own preferred pathway in the network, and participates in the evolution of the energy landscape [27,30]. Several studies have demonstrated that the mixed alkali effect has a structural origin associated with a cationic potential energy mismatch effect. Such evidence is

* Corresponding author. Tel.: +45 9940 8522.
E-mail address: yy@bio.aau.dk (Y.Z. Yue).

obtained from X-ray absorption spectroscopy [34,35], nuclear magnetic resonance (NMR) spectroscopy [36,37], infrared spectroscopy [38,39], and neutron and X-ray scattering [40] measurements. The dynamic structure model has been supported by results from both reverse Monte Carlo modeling [40] and molecular dynamics simulations [29,41,42].

The mixed alkaline earth effect has primarily been investigated in silicate and aluminosilicate glasses due to the industrial importance of these systems, e.g., as chemically strengthened cover glasses in personal electronic devices [43] and for modern design purposes [5]. In silicate systems, the glass transition temperature exhibits a negative deviation from linearity when calcium is substituted for magnesium [11,44–46]. Also, in the same system, Vickers hardness has been shown to deviate positively from linearity and the liquid fragility index negatively [5,14,47]. Density, molar volume and the coefficient of thermal expansion all exhibit a linear dependence on composition [5,11]. These results qualitatively agree with those of mixed alkali glasses [4].

In a systematic investigation of glass properties and their dependence of the mixed cationic effect (i.e., when both alkali and alkaline earth ions co-exist), Byun et al. [48] conclude that no "simple mechanism" can be responsible for the observed nonlinearities. Moreover, they point out that the deviation from linearity of certain properties must be intimately connected with microscopic structural changes [48]. Hence, in order to reveal the origin of the observed deviations of glass properties from linearity, the accompanying structural changes must be known [48]. In literature, the mixed alkaline earth effect has been observed as nonlinearities in properties of various silicate [11,13,14,44–47,49,50], phosphate [12,51], and borate glasses [52]. However, to our best knowledge, the correlation between the mixed alkaline earth effect and structural changes has not yet been studied.

In this paper, we investigate both static and dynamic properties of sodium aluminosilicate glasses containing calcium and/or magnesium with respect to the mixed alkaline earth effect. We prepare eight glass compositions with a molar ratio between calcium and magnesium varying from 0 to 1. We measure static properties such as density, molar volume, refractive index, coefficient of thermal expansion, elastic moduli, and Vickers hardness, as well as dynamic properties such as glass transition temperature, configurational heat capacity, and liquid fragility index. The influence of the mixed alkaline earth effect on these properties is discussed based on structural information obtained from room temperature Raman and NMR spectroscopy measurements. Finally, we discuss the mixed alkaline earth effect in terms of topological changes of the networks by considering the dynamic structure model.

2. Experimental procedure

2.1. Sample preparation

The analyzed compositions of the sodium aluminosilicate glasses under study are given in Table 1. All glasses included ~0.16 mol% SnO_2 as a fining agent. To prepare the glasses, the raw materials were first melted in a covered platinum crucible for 5 h in air at a temperature between 1450 and 1600 °C, depending on composition. In order to ensure chemical homogeneity, the melts were first quenched in water, and the resulting glass pieces were crushed and remelted for 6 h at 1650 °C and finally cast onto a stainless steel plate in air. The glasses were annealed for 2 h at their respective annealing points. The chemical compositions of the final glasses were determined using X-ray fluorescence, and the analyzed compositions were all within 0.5 mol% of the nominal targets (Table 1). Room-temperature densities of the glasses were determined by Archimedes' principle using water as immersion liquid.

2.2. Thermal expansion and strain, annealing, and softening points

Analysis of annealing and strain points involves heating a glass fiber of specific dimensions under a specific load (ASTM C336). The fibers

Table 1
Analyzed chemical composition of the eight sodium aluminosilicate glasses under study. Compositions were analyzed by X-ray fluorescence (± 0.1 mol%).

Glass ID	Composition (mol%)				
	SiO_2	Al_2O_3	Na_2O	MgO	CaO
Mg–Ca0	59.92	15.98	15.77	8.08	0.09
Mg–Ca0.8	59.93	15.98	15.83	7.33	0.78
Mg–Ca1.6	60.11	15.96	15.82	6.39	1.57
Mg–Ca2.4	59.91	15.99	15.79	5.76	2.40
Mg–Ca3.2	59.73	16.00	15.75	5.14	3.23
Mg–Ca4.8	59.81	16.02	15.70	3.41	4.90
Mg–Ca6.4	59.85	15.97	15.85	1.65	6.52
Mg–Ca8	59.83	16.01	15.79	0.13	8.08

were heated to approximately 25 K above their estimated annealing point and then cooled at a rate of 4 K/min. Annealing and strain points ($\eta = 10^{12.2}$ Pa s and $\eta = 10^{13.5}$ Pa s) were then determined as the temperatures that correspond to specific elongation rates, which have been identified by prior analysis of NIST standard glasses. Softening points ($\eta = 10^{6.6}$ Pa s) were determined by heating glass fibers and monitoring their elongation rate under their own weight (ASTM C338). The heating rate was set to 5 K/min and the softening point was defined as the temperature at which the elongation rate was 1 mm/min. Coefficients of thermal expansion (α) were also determined from this experiment, averaged over a temperature range of 25–300 °C.

2.3. Temperature dependence of viscosity

The temperature dependence of equilibrium viscosity was measured by performing beam bending, parallel plate, and concentric cylinder experiments. The viscosity curve of each composition is represented by data points at $10^{6.6}$ Pa s (obtained via parallel plate viscometry), 10^{11} Pa s (obtained via beam bending viscometry), and 12–20 data points in the range of 10^1 to 10^6 Pa s (obtained via the concentric cylinder method). For beam bending experiments, bars of 55 mm length and 2.5×2.5 mm^2 cross section were cut from the bulk glasses. For parallel plate experiments, cylinders of 6.0 mm diameter and 5.0 mm thickness were core drilled, and afterwards the flats were polished to an optical finish. For concentric cylinder experiments, ~600 g of crushed glass was remelted. The temperature errors associated with determining the 10^{11} Pa s point by the beam-bending method and the $10^{6.6}$ Pa s point by the parallel plate method are ± 1 and ± 2 °C, respectively. The estimated error in viscosity for the high-temperature measurements (by the concentric cylinder method) is $\log \eta = \pm 0.02$ (η in Pa s).

2.4. Vickers microhardness

All of the prepared glass samples were polished to mirror image finish and Vickers microhardness (H_V) was measured using a Duramin 5 indenter (Struers A/S). A total of 30 indents were conducted on each sample using an indentation time of 10 s and an indentation load of 0.49 N. The measurements were performed in air at room temperature.

2.5. Elastic moduli

The elastic properties (Young's and shear moduli) were measured at room temperature using resonant ultrasound spectroscopy. Prisms of dimensions 10 mm × 8 mm × 6 mm were used to gather resonance spectra from 100 to 300 kHz. For each sample, the first five resonant peaks as a function of frequency resulting from excited resonant eigenmodes were used to calculate the elastic properties.

2.6. Refractive indices

Refractive index (n) measurements were performed at the sodium D-line (589.3 nm) using a low range Precision Refractometer (Bausch & Lomb) with a sodium arc lamp. The measurements were performed on 1.0 mm thick samples with polished surfaces that were cleaned prior to measurements with high purity ethanol. The standard deviation of n is around ± 0.0003.

2.7. Glass transition temperature and isobaric heat capacity

Calorimetric measurements were performed on a differential scanning calorimeter (DSC 449C, Netzsch) to determine the calorimetric glass transition temperature (T_g) and the jump in heat capacity during the glass transition (ΔC_p). Each sample was subjected to two up and downscans at 10 K/min to approximately 100 K above the glass transition temperature. The first scan reflects an unknown thermal history whereas the second scan reflects the standard thermal history of a cooling of 10 K/min [53]. A flow of 40 ml/min argon was used as protective gas and platinum crucibles were used for both sample and reference. In order to calculate the isobaric heat capacity (C_p) of the sodium aluminosilicate glasses, a sapphire standard of approximately the same weight was measured before the measurement of each sample.

2.8. Structural aspects

Raman spectra were collected at room temperature on glass samples that were optically polished to a thickness of 50–80 μm with parallel top and bottom surfaces. Grinding and polishing were done using 600 grit SiC sand paper and cerium oxide slurry. A LabRAM HR800 Raman microscope (Horiba Jobin Yvon) was used to collect the spectra by using a 532 nm Verdi V2 DPSS green laser as the probing light source. The experimental setup is described in detail by Guerette and Huang [54]. Following Refs. [55,56], we have removed the spectral background by fitting a second order polynomial to the spectral region between 1250 and 1550 cm^{-1} (where no Raman bands are present), extrapolating it to lower frequencies and subtracting it from each spectrum.

^{27}Al magic angle spinning (MAS) NMR experiments were conducted at 11.7 T (130.22 MHz resonance frequency) using a commercial spectrometer (VNMRS, Agilent) and a commercial 3.2 mm MAS NMR probe (Varian/Chemagnetics). Powdered glasses were packed into aluminum-free 3.2 mm zirconia rotors with sample spinning at 20 kHz. 0.6 μs radio-frequency pulses, corresponding to a π/12 tip angle, were used to excite the ^{27}Al central transitions uniformly and thus provide quantitatively accurate Al speciation. The ^{27}Al MAS NMR spectra were processed without additional line broadening and referenced to aqueous aluminum nitrate at 0.0 ppm. ^{27}Al MAS NMR spectra were analyzed using the Dmfit program [57]. This program provides a means by which to simulate second-order quadrupolar lineshapes, and in the case of ^{27}Al NMR spectra, an additional parameter (Czjzek distribution) to account for distributions in the quadrupolar interaction [58]. ^{27}Al MAS NMR spectra were fit using this approach and relative peak intensities were determined from numerical integration of the simulated AlO$_4$ and AlO$_5$ lineshapes.

3. Results

3.1. Dynamic properties

The viscosity–temperature relationship has been the focus of several models [59–62]. Recently, Mauro et al. [61] proposed a new and improved model. This model is referred to as the "MYEGA" equation. It is founded upon the temperature dependence of configurational entropy [60] via the Adam–Gibbs equation of viscosity [59] and is derived based on topological constraint theory. The model is able to account for the configurational entropy both at the high temperature limit (a problem with the Avramov–Milchev model [60]) and at the low temperature limit (a problem with the Vogel–Fulcher–Tammann model [62]). Another important feature is that all three fitting parameters of the MYEGA model bear a physical meaning. The model is given by Eq. (1),

$$\log \eta(T) = \log \eta_\infty + (12 - \log \eta_\infty) \frac{T_g}{T} \exp\left[\left(\frac{m}{12 - \log \eta_\infty} - 1\right)\left(\frac{T_g}{T} - 1\right)\right] \quad (1)$$

where η_∞ is the high-temperature limit of liquid viscosity, T_g is the glass transition temperature, and m is the liquid fragility index. m is defined as the slope of an Angell plot at T_g (Eq. (2)) [63].

$$m \equiv \left. \frac{\partial(\log \eta(T))}{\partial(T_g/T)} \right|_{T=T_g} \quad (2)$$

By fitting Eq. (1) to the experimental viscosity data using a Levenberg–Marquardt algorithm [64,65] (see inset of Fig. 1), we obtain the liquid fragility index and glass transition temperature.

In Fig. 1, m is plotted as a function of the molar ratio of magnesium to total alkaline earth content [MgO] / ([MgO] + [CaO]). We note that two distinct compositional regimes exist. Initially, as calcium is substituted for magnesium, the liquid fragility index decreases. This trend continues until a substitution degree of 0.70 after which the fragility increases upon further substitution. The largest deviation from linearity (the dashed line) is observed at a substitution degree of ~0.63, i.e., the largest mixed alkaline earth effect is observed at a composition close to the one with equal concentrations of the two alkaline earth ions.

Fiber elongation data are presented in Figs. 2 and 3. In Fig. 2, the coefficient of thermal expansion (α), calculated as an average from 25 to 300 °C, is plotted as a function of the molar ratio of magnesium to total alkaline earth content. α exhibits a linear decrease over the entire composition range, with a minimum at a ratio of magnesium to total alkaline earth content equal to 1. The fitted linear tendency has an adjusted coefficient of determination (R^2) equal to 0.960. Isokom temperatures at the softening ($\eta = 10^{6.6}$ Pa s), annealing ($\eta = 10^{12.2}$ Pa s), and strain points ($\eta = 10^{13.5}$ Pa s) are plotted as a function of the molar ratio of magnesium to total alkaline earth content in Fig. 3. The dashed lines are guides for the eye and represent linear tendencies between the end-member glasses, whereas the solid lines represent polynomial fits
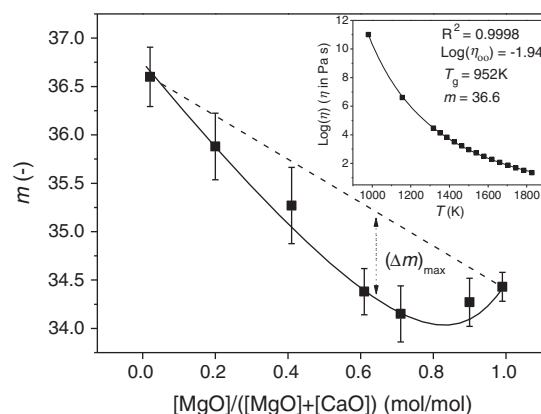
Fig. 1. Liquid fragility index (m) as a function of the molar ratio of magnesium to total alkaline earth content [MgO] / ([MgO] + [CaO]). m is determined by fitting the MYEGA equation (Eq. (1)) to the measured log η vs. T data. The inset shows an example of this determination using data for Mg-Ca8 [61]. The solid line represents the apparent relation between m and the molar ratio of [MgO] / ([MgO] + [CaO]), whereas the dashed line represents a linear relation between the two end-member compositions. Both lines are guides for the eye. $(\Delta m)_{max}$ is equal to the maximum discrepancy in fragility between the linear relation and the apparent relation, i.e., the largest mixed alkaline earth effect.
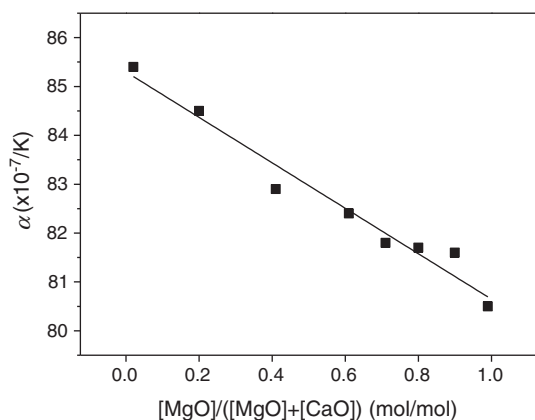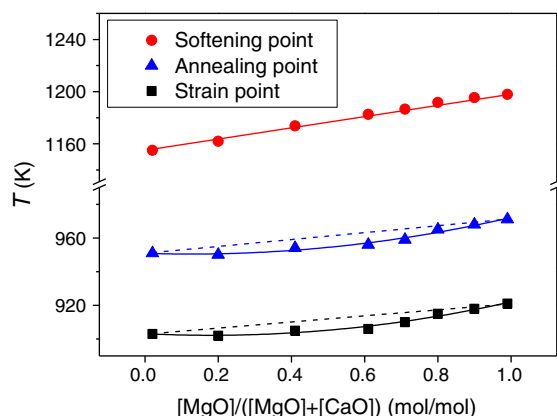
Fig. 2. Coefficient of thermal expansion (α) as a function of the molar ratio [MgO] / ([MgO] + [CaO]). α is taken as the average value between 25 and 300 °C. The solid line is a linear fit to data ($R^2 = 0.960$) and the accuracy of α is approximately $\pm 0.6 \times 10^{-7}$/K.

to all data points. Both the strain and the annealing points generally lie beneath the dashed line, since they exhibit a more parabolic shape, whereas the softening temperatures exhibit linear composition dependence and thus lie on the dashed line. Furthermore, both the straining and annealing isokoms have the largest deviation from linearity at a substitution degree of approximately 0.51. For all three points, the isokom temperature increases as magnesium is substituted for calcium. With an increase in isokom temperature, i.e., a decrease in viscosity, the deviation from linearity becomes less pronounced and approaches zero (Fig. 3). In other words, the mixed alkaline earth effect is declining as the temperature increases.

3.2. Physical properties

Vickers hardness (H_V) is determined by using the microindentation method. Experimental H_V values depend on the measurement conditions [66–69]. Consequently all microindentation experiments have been performed on the same indenter with the same indentation load and time (0.49 N and 10 s), ensuring crack free indents. Fig. 4 shows Vickers microhardness plotted as a function of the molar ratio of magnesium to total alkaline earth content. The dashed line represents a linear relationship between the end-member compositions. A parabolic fit

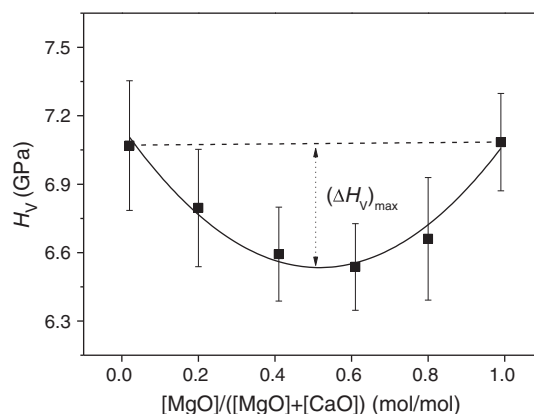matches the data well, and the largest deviation from linearity is found at a substitution degree of 0.50.

According to the Yamane and Mackenzie model [70] the elastic moduli control the deformation of glasses during microindentation. Therefore, shear modulus (G) and Young's modulus (E) have been determined and the results are shown in Fig. 5. It is seen that elastic moduli are compositionally invariant within the measured set of glasses, since both shear modulus and Young's modulus are constant within the error range for all measured compositions. Since the glass is isotropic, this means that the bulk modulus and Poisson's ratio must also be constant. In Fig. 6, density and molar volume at room temperature are plotted as a function of the molar ratio of [MgO] to [CaO] + [MgO]. The molar volume is calculated as the molar mass is divided by the glass density. Both density and molar volume exhibit a linear decrease as magnesium is substituted for calcium. The measured refractive indices (n) at 589.3 nm reveal the same linear tendency, i.e., n decreases as magnesium is exchanged with calcium (Fig. 7).

3.3. Thermodynamic fragility

The measured differential scanning calorimetry (DSC) curves are shown in Fig. 8. The composition dependence of the measured difference in heat capacity between supercooled liquid and glass (ΔC_p, an indirect measure of thermodynamic fragility) and glass transition temperatures (T_g) are shown in Figs. 9 and 10, respectively. These values were determined from the C_p–T curves obtained during the second DSC upscan as shown in the inset of Fig. 10 [52]. The dependence of T_g on [MgO] / ([MgO] + [CaO]) deviates negatively from linearity (dashed line), with the largest deviation at a substitution degree of 0.54 (Fig. 10). T_g increases with increasing substitution of calcium for magnesium. The thermodynamic fragility exhibits two regions of composition dependence. At low magnesium concentration, ΔC_p decreases as calcium is substituted for magnesium, whereas at low calcium concentrations, ΔC_p increases. The slope changes from negative to positive at [MgO] / ([MgO] + [CaO]) = 0.70 and the largest deviation from linearity is at [MgO] / ([MgO] + [CaO]) = 0.49.

3.4. Structural aspects

Raman spectra of representative sodium aluminosilicate glasses are shown in Fig. 11, where the Raman intensity is plotted as a function of wavenumber (ν). The two low-wavenumber peaks are both unaffected by composition variations, i.e., all samples have peaks positioned at $\sim$498 cm^{-1} and $\sim$570 cm^{-1}, respectively. According to Galeener [71]

Fig. 3. Strain ($\eta = 10^{13.5}$ Pa s), annealing ($\eta = 10^{12.2}$ Pa s), and softening point ($\eta = 10^{6.6}$ Pa s) as a function of the molar ratio [MgO] / ([MgO] + [CaO]). Data is measured by fiber elongation. The dashed lines represent linear relations between the isokom temperatures and the magnesium to total alkaline earth content. The solid lines are polynomial fits [64,65]. The uncertainty in the determinations of the straining and annealing points are ± 2 K and ± 3 K for the determination of softening points, i.e., errors are smaller than the size of the symbols.

Fig. 4. Vickers microhardness (H_V) as a function of the molar ratio [MgO] / ([MgO] + [CaO]). The solid line represents the apparent relation between H_V and the molar ratio of [MgO] / ([MgO] + [CaO]) whereas the dashed line is a linear extrapolation between the end-member compositions; both are guides for the eye. $(\Delta H_V)_{max}$ is marked on the figure as where the largest discrepancy is between linear relation and apparent relation, i.e., the largest mixed alkaline earth effect.
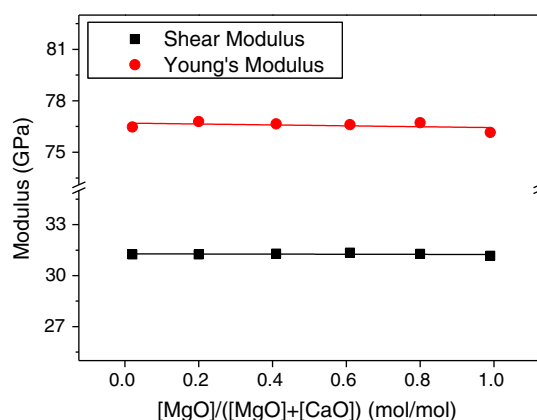
Fig. 5. Elastic moduli as a function of the molar ratio [MgO] / ([MgO] + [CaO]). The solid lines are linear fits. Both Young's modulus and shear modulus are determined by resonant ultrasound spectroscopy experiments. The uncertainty of this method is approximately ±0.2 GPa.

Fig. 7. Refractive index (n) measured at 589.3 nm as a function of the molar ratio [MgO] / ([MgO] + [CaO]). The solid line is a linear fit to data with $R^2 = 0.998$. The standard deviation of n is around ±0.0003.
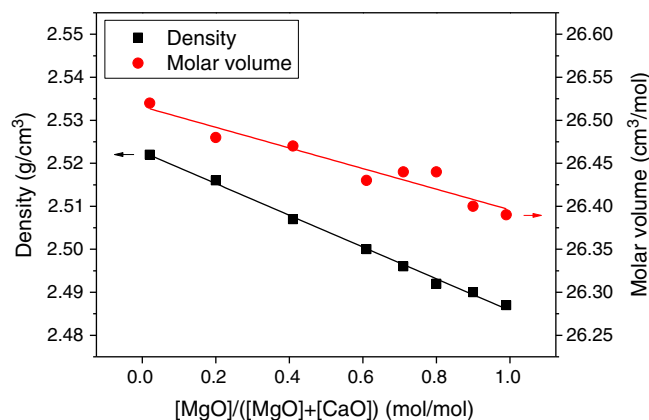
these peaks are caused by silicon–oxygen–silicon bending vibrations of threefold and fourfold silica ring structures embedded in the glass network. The position of the high-wavenumber band, ~1000 cm^{-1}, varies as magnesium is exchanged with calcium (Fig. 12). According to McMillan [72], this peak is associated with silicon–oxygen stretching vibrations of tetrahedral silicate units. The dashed line in Fig. 12 represents a linear relation between the end-member compositions. We find that the peak position diverges positively from a linear tendency, with the largest deviation found at [MgO] / ([MgO] + [CaO]) = 0.63.

MAS NMR spectra of ^{27}Al in representative sodium aluminosilicate glasses under study are shown in Fig. 13. The spectra all exhibit a narrow asymmetric peak centered around +50 ppm, consistent with tetrahedral aluminum groups (Al^{IV}) [73]. The aluminum speciation of these glasses is thus very similar to each other, since both position and shape of the ^{27}Al resonance exhibit only minor composition dependence. Only the spectrum of the magnesium end-member composition is slightly broader and more asymmetric on the more shielded side (lower shift). This is due to the presence of higher Al coordination in this sample, such as five-fold coordinated aluminum (Al^{V}).
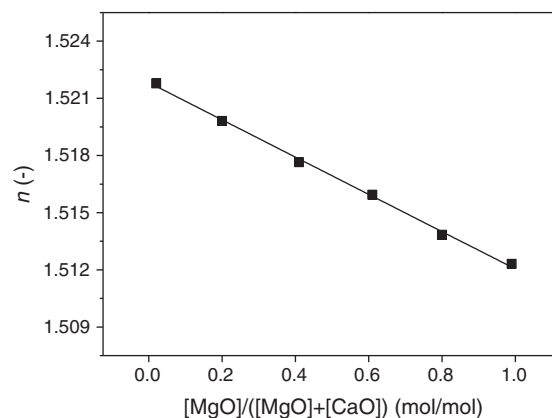
4. Discussion

4.1. Effect of alkaline earth field strength

In this section, we discuss the effects of completely substituting magnesium for calcium on selected physical properties, i.e., we focus

on the difference between the two single alkaline earth-containing end-member compositions.

The high wavenumber vibrational modes of Raman spectroscopy could be associated with higher network connectivity because more energy is required to induce atomic vibrations (shifts in the Q^n-value of the tetrahedral SiO$_4$ units). Since the oxygen coordination number of Mg^{2+} is probably lower than that of Ca^{2+} [74–76], the number of affected oxygen ions in the SiO$_4$ network decreases when substituting Mg^{2+} for Ca^{2+}. This explains why the concentration of T–O–T bonds (T = tetrahedral unit) increases as magnesium is substituted for calcium (Fig. 12). It is also well established that tetrahedrally coordinated Mg^{2+} can act as a network former, contributing to an increased population of T–O–T bonding at higher magnesium contents [77].

The magnesium-containing glass has lower density and smaller molar volume compared to the calcium-containing glass (Fig. 6). This difference in molar volume reflects a modification of the glass network structure. The smaller molar volume is caused by tighter binding of oxygen to magnesium, as expected from the larger field strength and smaller size of magnesium compared to calcium [12,78]. It should be noted that a smaller molar volume does not correspond to a denser structure. In contrast, the structure becomes less dense indicated by a decrease in the refractive index when substituting calcium for magnesium (Fig. 7). Hence, although Mg^{2+} has shorter and stronger cation–oxygen bonds, the overall atomic densities of these glasses are lower than that of the ones containing Ca^{2+}.

Vickers hardness is a measure of the resistance towards mechanical deformation of the glass and is phenomenologically related to

Fig. 6. Density and molar volume as a function of the molar ratio [MgO] / ([MgO] + [CaO]). The solid lines are linear fits to data with R^2 equal to 0.996 and 0.912 for density and molar volume, respectively. Uncertainties in both values are smaller than the symbol sizes.
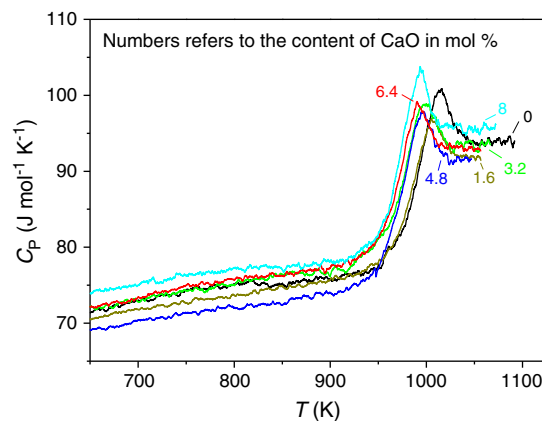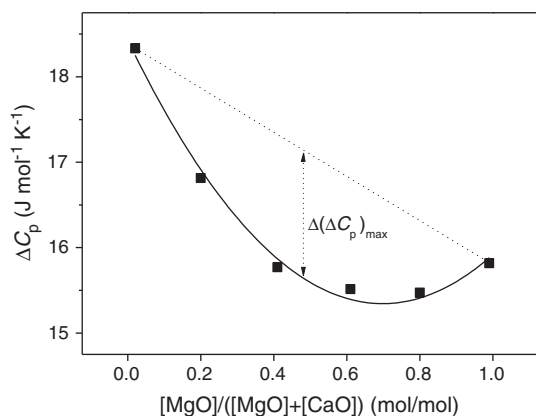

Fig. 8. Heat capacity as a function of temperature for the six samples with different CaO contents (in mol%) as indicated in the figure. The composition of each sample is given in Table 1. The heat capacities are determined by differential scanning calorimetry at a heating rate of 10 K/min subsequent to a cooling of 10 K/min.

Fig. 9. ΔC_p as a function of the molar ratio of [MgO] / ([MgO] + [CaO]). ΔC_p is the jump in heat capacity occurring at the glass transition and it is calculated as the heat capacity at the glass transition offset (C_{pl}) minus the heat capacity at the glass transition (C_{pg}). An illustration of how to determine these characteristic heat capacities is shown in the inset of Fig. 10. The uncertainty of this method is around ± 0.3 J mol^{-1} K^{-1}. The solid line represents the apparent relation between ΔC_p and the molar ratio of [MgO] / ([MgO] + [CaO]), whereas the dashed line represents a linear extrapolation between the end-member compositions. Both lines are guides for the eye. $\Delta(\Delta C_p)_{max}$ is equal to the maximum discrepancy in ΔC_p between the linear relation and the apparent relation, i.e., the largest mixed alkaline earth effect.

three different deformation mechanisms: densification, elastic deformation, and plastic flow [79]. The elastic moduli of the measured glasses show no compositional dependence (Fig. 5), so according to Yamane and Mackenzie [70] the elastic resistance in these systems should be compositionally invariant. This is in good agreement with the fact that the two end-member compositions exhibit identical hardness. Furthermore, it is expected that the magnesium composition is *less* susceptible to densification based on its lower molar volume [70,80]. However, the magnesium composition has a lower refractive index compared to the calcium composition, indicating that the former composition is *more* susceptible to densification [81]. Both density and refractive index only show minor composition variation (± 1–2%). Thus, it is likely that densification is also compositionally independent within the studied composition range. Plastic flow has earlier been argued to take place above a certain concentration of network modifiers [82]. As both end-member compositions contain the same amount of alkali and alkaline earth oxides, the plastic flow should be identical, and hence, both have similar Vickers hardness (Fig. 4).
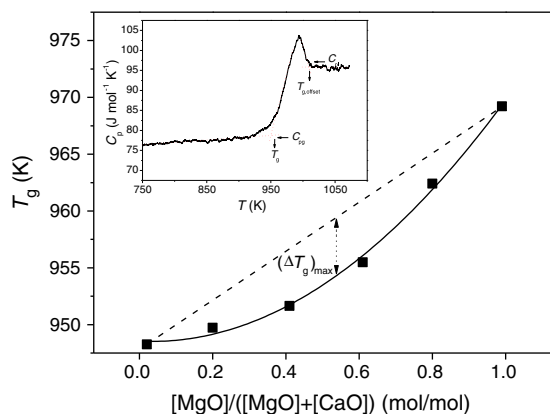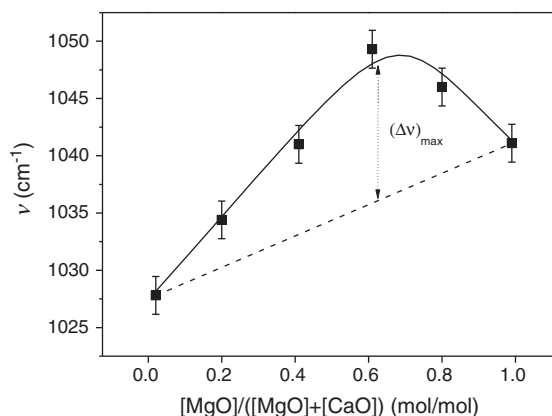

Fig. 10. The glass transition temperature from differential scanning calorimetry as a function of the molar ratio of [MgO] / ([MgO] + [CaO]). The solid line represents the apparent relation between T_g and the molar ratio of [MgO] / ([MgO] + [CaO]), whereas the dashed line is a linear relation; both are guides for the eye. $(\Delta T_g)_{max}$ is marked on the figure where the largest discrepancy exists between linear relation and apparent relation, i.e., the largest mixed alkaline earth effect. Inset: Method for determining T_g and characteristic heat capacities from the heat capacity curves measured by differential scanning calorimetry [53]. The uncertainty of this method is ± 2–3 K [88].
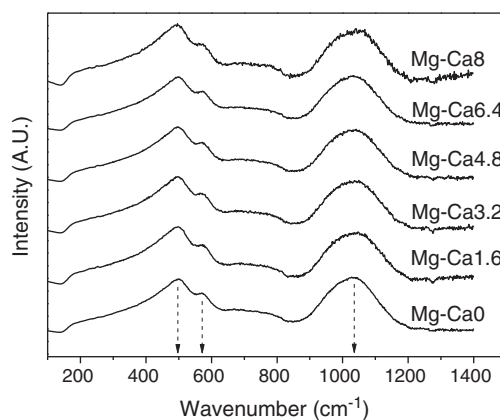

Fig. 11. Raman spectra for the sodium aluminosilicate glasses. The spectra are shifted vertically for clarity. The composition of each sample is tabulated in Table 1, with the designation written on the right corresponding to a specific composition. The arrows indicate the approximate peak positions.

The liquid fragility is closely related to the microstructure of glasses and liquids. Usually for oxide compositions, at temperatures above T_g, *strong* liquids contain a high degree of connectivity and *fragile* ones a comparably low degree of connectivity [63]. More precisely, strong liquids have a medium-range structure which is more stable towards temperature fluctuation around T_g. As shown in Figs. 1 and 9, kinetic and thermodynamic fragilities both exhibit the same composition dependence, viz., a decrease in fragility as magnesium is substituted for calcium. As discussed above, the higher field strength of magnesium increases the amount of rigid constraints at T_g and hence, results in lower fragility indices. This is supported by the Raman spectroscopic data, which imply stronger bonding in the magnesium end-member composition.

The higher field strength of magnesium is correlated with a deeper potential energy well, resulting in a decrease of the magnitude of the anharmonic vibrations at a given temperature, and thus, also a decrease of the coefficient of thermal expansion [48]. This agrees with the findings reported in Fig. 2, where α is found to decrease when substituting magnesium for calcium. It is generally accepted that T_g is mainly determined by both the connectivity of the network and its average bond strength. This is supported by accurate quantitative T_g predictions using temperature-dependent constraint theory [83,84]. In our case, the fragility, α, and Raman spectroscopic data suggest a stronger network, i.e., more rigid constraints, in the Mg^{2+} containing compositions. Hence, the higher bond strength between magnesium and oxygen is

Fig. 12. Peak position wavenumber (ν) of the Raman peak near 1050 cm^{-1} as a function of the molar ratio [MgO] / ([MgO] + [CaO]). The solid line represents the apparent relation between ν and the molar ratio of [MgO] / ([MgO] + [CaO]), whereas the dashed line represents a linear relation between the end-member compositions. Both lines are guides for the eye. $(\Delta\nu)_{max}$ is equal to the maximum discrepancy in ν between the linear relation and the apparent relation, i.e., the largest mixed alkaline earth effect.
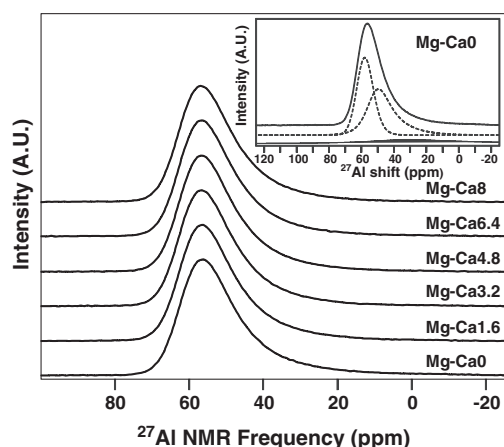
Fig. 13. ^{27}Al MAS NMR spectra for the six selected glasses. The spectra show unchanging lineshape for all glasses expect the magnesium end-member composition, which is slightly broader on the more shielded side. The inset shows an example of deconvoluting these data into Al^{IV} (dashed lines) and Al^{V} peaks (filled area), allowing for an estimation of changes in Al coordination [85]. Multiple Al^{IV} resonances were required to account for the complex lineshape and are consistent with literature values for isotropic chemical shift and quadrupolar coupling product in sodium aluminosilicate and alkaline earth aluminosilicate glasses. The fitting parameters for the Al^{V} resonance match those used in Ref. [85].

overcompensating the smaller coordination number [12], resulting in a higher T_g (Fig. 10). In other words, compared to calcium, magnesium has more rigid constraints at the temperatures of measurement (sub-T_g). The explanation is that some magnesium constraints have a higher onset temperature than those of calcium, which results in more rigid constraints at sub-T_g temperatures, even though the coordination number of magnesium is lower than that of calcium. The same phenomenon is responsible for the increase in isokom temperatures (Fig. 3), because an increase in isokom temperature corresponds to an increase in viscosity (for a constant temperature below T_g). This observation is in agreement with the overall trends of the Raman spectroscopic data, fragility and glass transition temperature data, all suggesting stronger oxygen bonding, more rigid constraints, and more tetrahedral bonding in the magnesium-containing compositions. From the NMR data (Fig. 13), we conclude that AlO$_4$ tetrahedra in the Ca-containing glasses are essentially all charge-balanced by a combination of Na$^+$ and Ca^{2+}. These spectra can be satisfactorily simulated without the need for an Al^V resonance. However, in the one instance where Ca is only present at trace levels, the need for alkaline earth cations (Mg^{2+}) to complement the role of Na$^+$ is partially ineffective, leading to a small population of Al^V species. In detail we find approximately 5% Al^V in the Mg–Ca0 composition compared to 0% in the remaining compositions (see inset of Fig. 13). Such quantities of Al^V species are consistent with high quality fitting of ^{27}Al MAS NMR spectra in similar systems [58,85]. Changes in aluminum speciation in the mixed alkaline earth compositions are thus negligible, even though we measure a slight increase of the connectivity in the magnesium-containing end-member composition. This slight increase in Al^V of the magnesium-containing composition contributes to the general trend, being that the magnesium-containing composition compared to the calcium-containing one has higher T_g, isokom temperatures and fragility, i.e., properties related to the connectivity.

4.2. Mixed alkaline earth effect

The mixed alkaline earth effect is observed as a deviation from linear composition dependence. For the current glasses under investigation, we find the effect manifested in the Raman spectroscopic data (Fig. 12) as a maximum and in the Vickers hardness (Fig. 4), fragility (Figs. 1 and 9), glass transition temperature (Fig. 10) and viscosity data (Fig. 3) as a minimum. According to Fluegel [78], the mixed

alkaline earth effect is normally observed as a minimum in viscosity. He observed a gradient in the slope of the viscosity-composition plot, going from a large negative departure at low concentration of modifier to a relatively small slope at high concentration of modifier. Neuville and Richet [49] explain the minima in viscosity by an excess of entropy caused by mixing, however, this behavior is in complete contrast to the theory given by Dietzel [3]. The theory by Dietzel [3] is that oxygen stabilized by two different alkaline earth ions is energetically much more favored than oxygen stabilized by similar alkaline earth ions [50], which should result in *maxima* in Vickers hardness, isokom temperatures and T_g. The observed *minima* in Vickers hardness (Fig. 4), isokom temperatures (Fig. 3), and T_g (Fig. 10) indicate the exact opposite, namely that the mixed magnesium–calcium compositions experience weaker bonding than the end-member compositions.

Above we argued that both densification and elastic deformation are compositionally independent. This suggests that plastic flow accounts for the nonlinear composition dependence of Vickers hardness [6,86]. Faivre et al. [6] reported that the plastic flow of glass is caused by the hopping of network modifiers, promoting slippage of the rigid parts of the network [82,86]. This is, however, not the entire explanation, as we may assume that the plastic flow is generated by a more cooperative rearrangement of atoms. Ionic conductivity measurements reveal a minimum in conductivity as one alkaline earth ion is substituted for another one [1]. Hence, the lowest concentration of mobile ions is at a substitution degree of 0.50 and the plastic flow according to Faivre et al. [6] should therefore have a minimum at this composition. The minimum in ionic conductivity at equal concentrations of alkaline earth ions is also predicted by the dynamic structure model [30,33]. This is, however, not what we observe in Fig. 4, since a *minimum* in ionic conductivity should correspond to a *maximum* in hardness. If we instead consider viscosity to be an estimate of the plastic flow, we suggest that the occurrence of the minimum in hardness is associated with the corresponding minimum in isokom temperatures. Although the deformation under indentation and the viscous flow under shear occur at various temperature regions, their mechanisms are similar to large extents, i.e., both are related to the translational motion of structural units. It can be argued that the responsible underlying topological constraints of the mechanisms may differ, due to the temperature dependence of these constraints. If this is the case, an offset might occur between the minima in Vickers microhardness and isokom temperatures at room-temperature [87].

Based on the Raman spectroscopic data, we find a relatively high concentration of T–O–T bonds in the mixed alkaline earth region (Fig. 12). This might be associated with the observed negative deviation from linearity for the liquid fragility index, since higher network connectivity generally corresponds to a *stronger* liquid. However, the low-temperature viscosity of the mixed alkaline earth compositions is lower than that of the end-member compositions (Fig. 3). The Raman spectroscopic data suggest that the network connectivity of the mixed Ca–Mg compositions is higher than that of the two end-members, which normally increases viscosity. Therefore we can infer that the decrease of viscosity observed in this work is not related to the network connectivity, but instead is mainly related to the local structural environment around the network modifiers causing overall bond weakening.

5. Conclusion

We have studied the mixed alkaline earth effect in a series of MgO/CaO sodium aluminosilicate glasses by substituting MgO for CaO. We find that the mixed alkaline earth effect manifests itself as a maximum in T–O–T bonds, but a minimum in Vickers microhardness, glass transition temperature, and isokom temperatures. We explain the minimum in viscosity by a bond weakening in the local structural environment around the network modifiers, viz., the minimum originates from the structural character of the modifying ions.

The viscous flow under shear and deformation under indentation are both related to the translational motion of structural units, and

since the elastic moduli in the investigated system are compositionally independent, we suggest that the observed minimum in microhardness is associated with the corresponding minimum in shear viscosity.

Acknowledgments

References

[1] Y. Gao, C. Cramer, Solid State Ionics 176 (2005) 921.
[2] A. Mohajerani, J.W. Zwanziger, J. Non-Cryst. Solids 358 (2012) 1474.
[3] A.H. Dietzel, Phys. Chem. Glasses 24 (1983) 172.
[4] D.E. Day, J. Non-Cryst. Solids 21 (1976) 343.
[5] R.J. Hand, D.R. Tadjiev, J. Non-Cryst. Solids 356 (2010) 2417.
[6] A. Faivre, F. Despetis, F. Guilaume, P. Solignac, J. Am. Ceram. Soc. 93 (2010) 2986.
[7] G. Gehlhoff, M. Thomas, Z. Tech. Phys. (1926) 105.
[8] J.E. Shelby, D.E. Day, J. Am. Ceram. Soc. 53 (1970) 182.
[9] H.W. Guo, X.F. Wang, Y.X. Gong, D.N. Gao, J. Non-Cryst. Solids 356 (2010) 2109.
[10] J.O. Isard, J. Non-Cryst. Solids 1 (1969) 235.
[11] Y. Hasegawa, Glastech. Ber. 57 (1984) 177.
[12] K. Hirao, M. Yoshimoto, N. Soga, K. Tanaka, J. Non-Cryst. Solids 130 (1991) 78.
[13] K.-D. Kim, Glastech. Ber. Glass. Sci. Technol. 72 (1999) 393.
[14] M. Solvang, Y.Z. Yue, S.L. Jensen, J. Non-Cryst. Solids 345 & 346 (2004) 782.
[15] M.L.F. Nascimento, E. Nascimento, S. Watanabe, Mater. Chem. Phys. 96 (2006) 55.
[16] B. Roling, M.D. Ingram, J. Non-Cryst. Solids 265 (2000) 113.
[17] M.L.F. Nascimento, S. Watanabe, Mater. Chem. Phys. 105 (2007) 308.
[18] M.D. Ingram, A.H.J. Robertson, Solid State Ionics 94 (1997) 49.
[19] M.D. Ingram, C.T. Moynihan, A.V. Lesikar, J. Non-Cryst. Solids 38 & 39 (1980) 371.
[20] D. Wolf, J. Phys. Chem. Solids 40 (1979) 757.
[21] J.N. Mundy, Solid State Ionics 28–30 (1988) 671.
[22] D. Ravaine, J. Non-Cryst. Solids 73 (1985) 287.
[23] J.A. Bruce, M.D. Ingram, M.A. MacKenzie, Solid State Ionics 18 & 19 (1986) 410.
[24] S.R. Elliott, Solid State Ionics 27 (1988) 131.
[25] S.R. Elliott, Mater. Sci. Eng. B3 (1989) 69.
[26] K. Funke, Prog. Solid State Chem. 22 (1993) 111.
[27] A. Bunde, M.D. Ingram, P. Mass, J. Non-Cryst. Solids 172–174 (1994) 1222.
[28] M.D. Ingram, Physica A266 (1999) 390.
[29] S. Balasubramanian, K.J. Rao, J. Phys. Chem. 97 (1993) 8835.
[30] A. Bunde, M.D. Ingram, P. Maass, K.L. Ngai, J. Non-Cryst. Solids 131–133 (1991) 1109.
[31] J. Dyre, P. Maass, B. Roling, D.L. Sidebutton, Rep. Prog. Phys. 72 (2009) 1.
[32] K.J. Rao, S. Kumar, Curr. Sci. 86 (2003) 945.
[33] P. Maass, R. Peibst, J. Non-Cryst. Solids 352 (2006) 5178.
[34] G.N. Greaves, K.L. Ngai, Phys. Rev. B52 (1995) 6358.
[35] S.N. Houde-Walter, J.M. Inman, A.J. Dent, G.N. Greaves, J. Phys. Chem. 97 (1993) 9330.
[36] B. Gee, M. Janssen, H. Eckert, J. Non-Cryst. Solids 215 (1997) 41.
[37] J.F. Stebbins, Solid State Ionics 112 (1998) 137.
[38] E.I. Kamitsos, A.P. Patsis, G.D. Chryssikos, J. Non-Cryst. Solids 152 (1993) 246.
[39] E.I. Kamitsos, Y.D. Yiannopoulos, H. Jain, W.C. Huang, J. Non-Cryst. Solids B54 (1996) 9775.
[40] J. Swenson, A. Matic, C. Karlsson, L. Börjesson, C. Meneghini, W.S. Howells, Phys. Rev. B63 (2001) 132202.
[41] H. Lammert, A. Heuer, Phys. Rev. B72 (2005) 214202.
[42] J. Habasaki, I. Okada, Y. Hiwatari, J. Non-Cryst. Solids 183 (1995) 12.
[43] A.K. Varshneya, Int. J. Appl. Glass Sci. 1 (2010) 131.
[44] G. Mingin, Z. Zhang, L. Ly, W. Xingen, Y. Ruifang, XIV Int. Cong. Glass, 357, 1986.
[45] J. Briggs, Glass Ceram. Bull. 22 (1975) 73.
[46] M.M. Smedskjaer, L. Huang, G. Scannell, J.C. Mauro, Phys. Rev. B85 (2012) 144203.
[47] S. Yoshida, J.-C. Sanglebœuf, T. Rouxel, J. Mater. Res. 20 (2005) 3404.
[48] J.-O. Byun, B.-H. Kim, K.-S. Hong, H.-J. Jung, S.-W. Lee, A.A. Izyneev, J. Non-Cryst. Solids 190 (1995) 288.
[49] D.R. Neuville, P. Richet, Geochim. Cosmochim. Acta 55 (1991) 1011.
[50] Y. Hasegawa, Glastech. Ber. 53 (1980) 277.
[51] R. Waesche, R. Brückner, J. Non-Cryst. Solids 107 (1989) 309.
[52] B.Z. Pevzner, V.P. Klyuev, Glass Phys. Chem. 30 (2004) 506.
[53] Y.Z. Yue, J.deC. Christiansen, S.L. Jensen, Phys. Chem. Lett. 357 (2002) 20.
[54] M. Guerette, L. Huang, J. Phys. D: Appl. Phys. 45 (2012) 275302.
[55] V.P. Zakaznova-Herzog, W.J. Malfait, F. Herzog, W.E. Halter, J. Non-Cryst. Solids 353 (2007) 4015.
[56] W.J. Malfait, W.E. Halter, Phys. Rev. B77 (2008) 014201.
[57] D. Massiot, F. Fayon, M. Capron, I. King, S. Le Calvé, B. Alonso, J.-O. Durand, B. Bujoli, Z. Gan, G. Hoatson, Magn. Reson. Chem. 40 (2002) 70.
[58] D.R. Neuville, L. Cormier, D. Massiot, Geochim. Cosmochim. Acta 68 (2004) 5071.
[59] G. Adam, J. Gibbs, J. Phys. Chem. 43 (1965) 139.
[60] I. Avramov, A. Milchev, J. Non-Cryst. Solids 104 (1988) 253.
[61] J. Mauro, Y.Z. Yue, A.J. Ellison, P.K. Gupta, D.C. Allan, Proc. Natl. Acad. Sci. U. S. A. 106 (2009) 19780.
[62] G.W. Scherer, J. Am. Ceram. Soc. 75 (1992) 1060.
[63] C.A. Angell, Science 267 (1995) 1924.
[64] D.W. Marquardt, J. Soc. Indust. Appl. Math. 11 (1963) 431.
[65] K. Levenberg, Quart. Appl. Math. 2 (1944) 164.
[66] R. Roeskiy, J.R. Varner, J. Am. Ceram. Soc. 74 (1991) 1129.
[67] H. Li, R.C. Bradt, J. Non-Cryst. Solids 146 (1992) 197.
[68] T. Kavetskyy, J. Borc, K. Sangwal, V. Tsmots, J. Optoelectron. Adv. Mater. 12 (2010) 2082.
[69] J.-M. Schneider, M. Bigerelle, A. Iost, Mater. Sci. Eng. A262 (1999) 256.
[70] M. Yamane, J.D. Mackenzie, J. Non-Cryst. Solids 15 (1974) 153.
[71] F.L. Galeener, J. Non-Cryst. Solids 49 (1982) 53.
[72] P. McMillan, Am. Mineral. 69 (1984) 622.
[73] S.H. Risbud, R.J. Kirkpatrick, A.P. Taglialavore, B. Montez, J. Am. Ceram. Soc. 70 (1987) C10.
[74] A.K. Katz, J.P. Glusker, S.A. Beebe, C.W. Bock, J. Am. Chem. Soc. 118 (1996) 5752.
[75] B.N. Nelson, G. Exarhos, J. Chem. Phys. 71 (1979) 2739.
[76] K. Shimoda, T. Nemoto, K. Saito, J. Phys. Chem. B112 (2008) 6747.
[77] S. Sen, H. Maekawa, G.N. Papatheodorou, J. Phys. Chem. B113 (2009) 15243.
[78] A. Fluegel, Eur. J. Glass Sci. Technol. A48 (2007) 13.
[79] J.A. Howell, J.R. Hellmann, C.L. Muhlstein, Mater. Lett. 62 (2008) 2140.
[80] T. Rouxel, T. Hammouda, A. Moréac, Phys. Rev. Lett. 100 (2008) 225501.
[81] T. Rouxel, H. Ji, J.P. Guin, F. Augereau, B. Rufflé, J. Appl. Phys. 107 (2010) 094903.
[82] K.W. Peter, J. Non-Cryst. Solids 5 (1970) 103.
[83] J.C. Mauro, P.K. Gupta, R.J. Loucks, J. Chem. Phys. 130 (2009) 234503.
[84] P.K. Gupta, J.C. Mauro, J. Chem. Phys. 130 (2009) 094503.
[85] D.R. Neuville, L. Cormier, V. Montouillout, P. Florian, F. Millot, J.-C. Rifflet, D. Massiot, Am. Mineral. 93 (2008) 1721.
[86] A. Mohajerani, J.W. Zwanziger, J. Non-Cryst. Solids 358 (2012) 1474.
[87] M.M. Smedskjaer, J.C. Mauro, Y.Z. Yue, Phys. Rev. Lett. 105 (2010) 115503.
[88] Q. Zheng, M. Potuzak, J.C. Mauro, M.M. Smedskjaer, R.E. Youngman, Y.Z. Yue, J. Non-Cryst. Solids 358 (2012) 993.